Analysis of the IC 443 Supernova Remnant with H.E.S.S. Data

Bachelorarbeit aus der Physik

Vorgelegt von
Lukas Großpietsch
29.08.2024

Erlangen Centre for Astroparticle Physics
Friedrich-Alexander-Universität Erlangen-Nürnberg

Betreuerin: Dr. Alison Mitchell

Abstract

IC 443 is one of the few observed supernova remnants interacting with a molecular cloud. This thesis is a first analysis of IC 443 observations with the H.E.S.S. telescope array using data taken from 2004 to 2005. The data show an extended source at $R.A. = 94.36^\circ \pm 0.04^\circ_{stat} \pm 0.006^\circ_{sys}$, $Dec. = 22.56^\circ \pm 0.03^\circ_{stat} \pm 0.006^{circ}_{sys}$ with $r_0 = 0.29^\circ \pm 0.03^\circ_{stat} \pm 0.006^\circ_{sys}$ at a significance of 4.12σ when fitting a disk spatial model. The geometry of the source is put into context by comparison with X-ray and radio observations by [1][2]. The obtained spectrum is best fit by a power law function $f(E) = A\left(\frac{E}{E_0}\right)^{-\alpha}$ with $E_0 = 1\,\mathrm{TeV}$, $\alpha = 3.0 \pm 0.14$, and $A = 8^{+3.1}_{-2.3} \times 10^{47}\,\mathrm{TeV}^{-1}$. A combined gamma-ray spectrum is obtained by adding the spectral energy distribution derived by the Fermi-LAT [3], MAGIC [4], and VERITAS [5]. This spectrum is best fitted by a broken power law function $A\left(E/E_0\right)^{-\alpha_1}$ for $E < E_{break}$ and $A\left({E_{break}/E_0}^{\alpha_2-\alpha_1}\right)\left(E/E_0\right)^{-\alpha_2}$ for $E > E_0$. The best fitted parameters are $\log_{10}(A) = 46.4 \pm 0.5$, $\alpha_1 = 2.31 \pm 0.02$, $E_0 = 6^{+4.0}_{-2.4}$, $\alpha_2 = 3.13 \pm 0.06$, and $E_{break} = 0.15 \pm 0.02$. This thesis finds that the combined spectrum can best be modeled by a parent proton population, indicated by the characteristic pion-bump.

Contents

1 Introduction

In July 1054, Chinese astronomers discovered a new star on the night sky which remained visible to them only until April 1056 after which it disappeared [6]. Even though they were unaware at the time, this is one of the first records of the explosion of a star, a so-called Supernova. This explosion was the birth of a pulsar and one of the most famous supernova remnants (SNRs), the Crab Nebula. After the remnant was discovered as a nebula, it was named after a drawing interpreted to be resembling a crab with arms in [7]. It is also the first source (M1) in Charles Messier's *Catalog of Nebulae and Star Clusters* [8] as he discovered it as a whitish light shaped like the flame of a candle while observing a comet in 1758. Since then it has been studied by many astronomers and has become of utmost importance to the entire field of astrophysics, nowadays even being used as a standard candle for detector calibration. Aided by the steady evolution of detection techniques and other technical advances, many more SNRs have been discovered since then.

These discoveries are of high scientific interest since the physical theories describing supernova explosions and the development of their remnants are highly complex and incomplete. Especially the creation of the often very intricate morphology of supernova remnants and the acceleration of particles in different areas of the remnant is highly useful in order to understand the production, propagation and acceleration of cosmic rays in the universe, since there is a multitude of physical phenomena involved. Within the initial supernova explosions and later at the shock fronts of the remnant, particles are accelerated to relativistic speeds, and through various interactions secondary very high-energy particles can be produced. These production mechanisms are described by the theories of high-energy particle physics which can be studied in particle accelerators on Earth. However, even the CERN Large Hadron Collider (LHC) can only accelerate protons to energies of 6.5 TeV [9] which are well below the limits of gamma-ray and cosmic-ray observatories on Earth. Therefore, high-energy particle physics depends on observations of supernovae and their remnants to understand the validity of our theories to the limits of very high energies.

The SNR analysed in the following chapters in the spectrum of high-energy gamma rays using data observed by the High Energy Stereoscopic System (H.E.S.S.) is the Jellyfish nebula or IC 443. A spatial and spectral analysis as well as physical modelling of the production mechanisms within the SNR to the observed spectrum will be conducted. The results will be discussed and put into context by considering further gamma-ray observations as well as data obtained at different wavelengths.

2 Supernova Remnants

2.1 Evolution of Supernova Remnants

Supernova Remnants (SNRs) are the remaining evidence of Supernovae, the explosive end of the lifetime of massive stars ($\sim 8\,M_\odot$) [10]. The energy freed in these events is stored in the envelopes of the dying star which are heated to very high temperatures and ejected at radial velocities of around $(10-20)10^3\,\mathrm{km/s}$. The shell remains at a constant velocity as long as the mass of the interstellar medium (ISM) swept up by the expanding sphere of stellar material is negligible in comparison to the ejected mass. Furthermore, the speed of the ejected sphere is larger than the speed of sound within the ISM leading to the formation of a shock wave and a contact discontinuity between shock front and the swept up ISM. In the simplest model, the temperature T of the ejected sphere decreases adiabatically as the sphere of radius R expands according to the relation $T \propto R^{-3(\gamma-1)}$ with γ the ratio of heat capacities before and behind the shock wave assuming a uniform temperature distribution. However, as the density in front of the shock wave is much larger than the density behind, the region between shock front and contact discontinuity is heated to high temperatures. Therefore, young supernova remnants are strong X-ray emitters. [11][12]

The second phase in the evolution of supernova remnants begins when the swept up mass becomes greater than the ejected mass. The overall dynamics are now determined by the total mass swept up and initial expanding gas and the energy released in the supernova explosion. The relation of sphere radius r to energy released in the explosion, density of the ISM and time t derived by Taylor and Sedov is: $r \propto (\frac{E}{\rho_0})^{\frac{1}{5}} t^{\frac{2}{5}}$. As the mass of the expanding shells increases significantly, they are decelerated leading to changes in temperature, density and pressure distribution. The outermost shell is decelerated first, generating an increasingly fast gas flow into the boundary region of the SNR. Once this gas flow becomes supersonic, a shock wave is formed at the inner edge of the compressed outer layers directed inward. The matter between this reverse shock wave and the outer edge is strongly reheated similarly to the first phase of the SNR evolution. Hence, intense soft X-rays are emitted from the outer layers. Furthermore, the structure of the SNR are Rayleigh-Taylor unstable and can therefore form undulations ("fingers") protruding from the respective layers as seen in e.g. Cassiopeia A and Tycho's SN. The interaction of the shock wave with atomic and molecular clouds leads to the emission of further cosmic rays in the form of relativistic electrons, protons, neutrinos or gamma-ray photons. This leads to SNRs interacting with molecular clouds being the largest number of detected galactic gamma-ray sources beyond Pulsars and PWNs. [12][11]

The SNR enters the third phase of its evolution once the temperature in the region behind the shock front drops below $10^6\,\mathrm{K}$. At these temperatures, cooling by the line emission of heavy ions becomes dominant and the shock front is compressed to preserve the pressure balance, forming the so called snow plough.

As the shock wave radiates most of its energy, it slows down further until it reaches subsonic velocities and becomes indistinguishable from the ISM. The material is then further dispersed into the interstellar space by random motion.

The collapsing core of the progenitor star undergoing the supernova forms a black hole or a neutron star depending on its mass. The mass limit of pulsars caused by the balance of neutron degeneracy pressure and gravity is $\sim 1.4\,M_\odot$ with possibly higher values for rapidly rotating neutron stars. Beyond this mass limit, the stellar core undergoing the Supernova evolves into a black hole. [11]

2.2 Gamma-ray production mechanisms

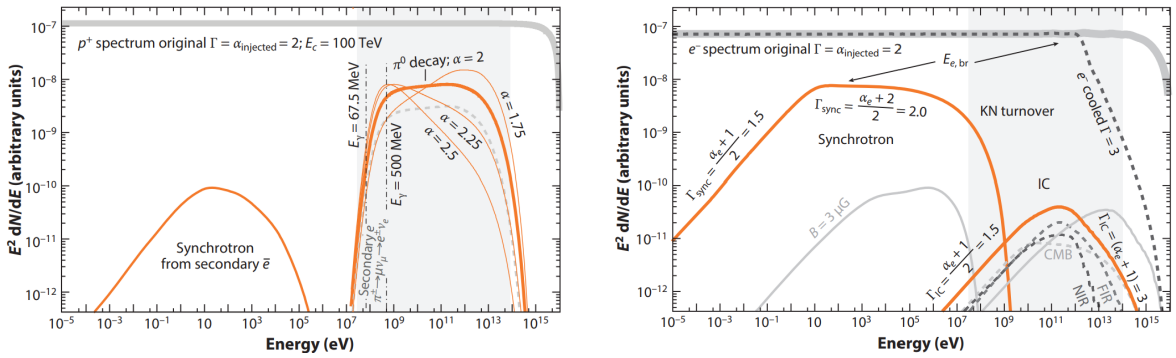

(a) (b)

Figure 1: Gamma-ray spectra for the hadronic (a) and leptonic (b) production mechanisms. The gray shaded region shows the energy range of current gamma-ray detectors (Fermi-LAT and IACTs). [12]

As discussed in the last section, SNRs radiate energy in the form of particles. Gamma rays are part of the emitted energy spectrum and can be detected on Earth. Within SNRs, different production mechanisms create characteristic spectra which can be used to identify the morphology of the source. On the one hand, the interaction of high energy electrons can produce gamma rays through synchrotron radiation or inverse compton scattering (see Figure 1). The resulting spectrum of this leptonic pathway has two peaks from the respective production mechanisms which can be distinguished when considering the energy range. Synchrotron radiation usually has a higher flux peak in the spectral energy distribution but sits at a lower energy than inverse compton scattering. The total detected spectrum contains contributions from both production mechanisms and shows a break energy at the transition from synchrotron to inverse compton radiation.

On the other hand, there is the hadronic production pathway of the pion decay. Protons from the spreading shells of the progenitor star are accelerated to relativistic speeds high enough for pion production when scattering inelastically with the ISM and especially higher density molecular clouds. Pions of all charges π^+, π^- and π^0 are created in this process. The positive and negative decay into positive and negative muons which in turn decay into relativistic positrons and electrons, emitting neutrinos in the process. The neutral pions decay into two gamma-ray photons at a mean energy of 180 MeV. The $E^2F(E)$ spectrum of this pion decay rises steeply to an energy of ~ 400 MeV and approximately mirrors the energy distribution of the parent proton population at higher energies greater than a few GeV, an aspect often regarded as the pion bump. This characteristic feature is the leading hint when determining the underlying production mechanism of a gamma-ray source since both production pathways are situated at similar energies. As the pion decay is induced by relativistic protons, this aspect is also evidence for these particles. At energies of $\sim 10^7 - 10^9$ eV, the slope of the spectrum produced by the leptonic pathways is far lower than the spectrum induced by pion decay. The shape of the spectrum directly mirrors the proton spectrum and therefore the energy of the relativistic protons can be directly inferred from the gamma-ray flux measured by the telescopes when assuming a given distance and density of the source region. For usual ratios of electrons to protons of $R \leq 10$, pion production dominates at high energies over leptonic production mechanisms. However, the

observed spectrum can always be a combination of the production mechanisms. [12]

Assuming pion decay and protons travelling at roughly the speed of light c, the energy emitted in gamma rays by a volume V filled uniformly with high energy particles and ISM is given by:

$$L_\gamma = \frac{1}{3}\sigma_{pp} N c \sum N_{CR}(E) E = \frac{1}{3} P_{coll} \epsilon_{CR} V \tag{1}$$

With σ_{pp} the cross section of the inelastic proton-proton scattering, N the number density of the ISM and N_{CR} the number density of high energy particles at the energy E. $P_{coll} = \sigma_{pp} N c$ is the probability of a proton undergoing an inelastic collision with a Nucleus of the ISM per second and ϵ_{CR} the local energy density of high energy particles. [11]

2.3 IC 443

IC 443, also known as the Jellyfish nebula, is a mixed morphology SNR created by the core collapse supernova which also created the pulsar CXOU J061705.3+222127 located within the nebula. This type of supernova remnant is defined to have a shell-like appearance in the radio spectrum while being centrally filled in X-rays [13]. IC 443 is also the first observation of a SNR interacting with a molecular cloud which was shown by the observation of strong molecular line emission regions. As SNRs interacting with molecular clouds are very bright in the spectrum of gamma rays, IC 443 is one brightest gamma-ray sources in our galaxy. The age of IC 443 is subject of ongoing discussions with many studies reporting an age of 20,000 to 30,000 years. The distance is assumed to be 1.5 kpc and is derived from filaments at the boundary of IC 443. [14][15][16]

The intricate morphology of IC 443 can best be observed in the spectra of X-ray and radio emissions. The radio observations described in the following section have been conducted by the Very Large Aray[1] (VLA), a ground based radio observatory located in New Mexico in the United States of America [2][17]. Furthermore, the X-ray observations of XMM-Newton[2] [18] and Chandra[3] [16], satellite mounted X-ray telescopes, are considered.

Studies of the 21 cm spectral line and radio continuum as well as optical observations show that IC 443 consists of two shells (A and B, see Figure 2) with distinctly different radial intensity distributions. The inner shell has a much harder defined edge while the outer shell has a soft boundary. In the southeastern region of the outer shell, there is a faint radio continuum halo and undulations ("spurs") where IC 443 overlaps with the remnant G189.6+3.3 (see Figure 3). The western part of shell B shows a breakout into rarefied medium. The southern boundary contains most of the shocked H_I gas which is blue-shifted. There is also a broad extended lane of unshocked H_I gas in the southern regions around the SNR. The H_I emissions furthermore show the strongest absorption around $v_{LSR} \sim -5\,\mathrm{km/s}$ which is associated to the systemic velocity of IC 443. Radio observations also show a few filament structures in the northeast of the SNR which can be explained by the shock wave propagating through a uniform medium of $n_H \sim 10\,\mathrm{cm}^{-3}$. X-ray as well as radio continuum observations also observe the Pulsar CXOU J061705.3+222127 and the associated PWN in the southern region of shell A. [2][16][17][18]

IC 443 has been first observed in gamma rays with EGRET in 1995 and subsequent observations by MAGIC, VERITAS and Fermi-LAT have been made. The center position derived by an analysis of MAGIC data is displaced in respect to the position found by EGRET (see Table 3) and is coincident with a large molecular cloud. The extended source regions of Fermi

[1] https://www.vla.nrao.edu/

[2] https://www.cosmos.esa.int/web/xmm-newton

[3] https://chandra.harvard.edu/

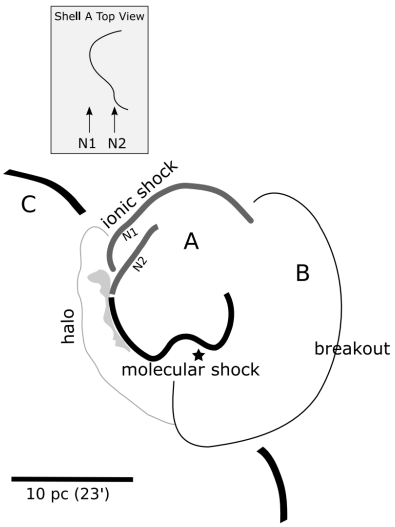

Figure 2: Schematic morphology of IC 443. The star denotes the position of the Pulsar proposed in [16]. Shells A and B, the radio continuum halo as well as shocked molecular and ionic shock regions are shown. The insert shows the proposed top view of shell A by [2]. Schematics from [2].

and VERITAS overlap almost completely and incorporate most molecular clouds and Shell A of the SNR as well as the pulsar and the PWN. Therefore contributions to the emission reported by Fermi and VERITAS can originate from all mentioned regions. The analyses performed on the studies of the Fermi-LAT also report a broad peak of the emission between a few 100 MeV and ~ 5 GeV which is consistent with the emission caused by neutral pion decay emitting gamma rays. [3][4][5][19][20]

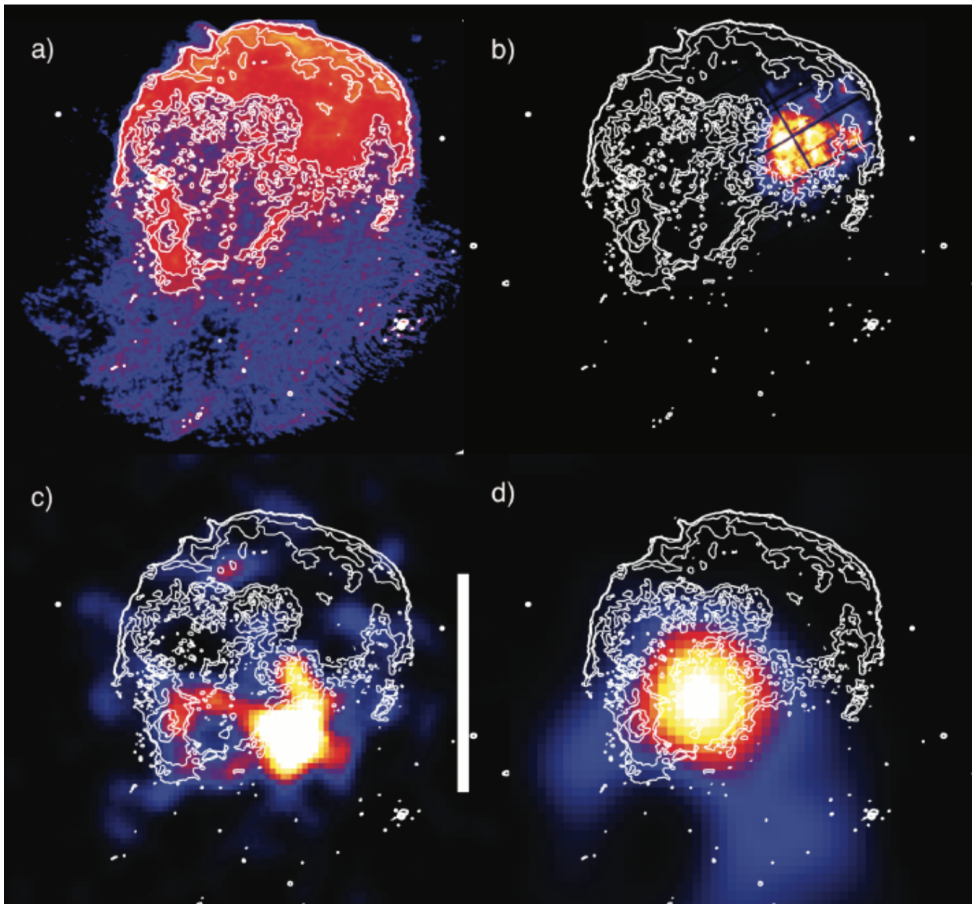

Figure 3: Multi wavelength comparison of IC 443. (a) VLA 330-Mhz continuum emission [17], (b) soft X-ray XMM observations (0.3-8 keV) [18], (c) Gev gamma-ray observations by Fermi-LAT [20] and (d) MAGIC observations above 380 GeV [4]. (a) shows the distinct shell in the northern regions of the SNR and the *spurs* in the southern regions. Image collection from [12]

3 Gamma-ray detection

There are three main groups of gamma-ray detectors: space telescopes mounted to satellites orbiting Earth, Imaging Atmospheric Cherenkov Telescopes (IACTs) which are ground based telescopes operating within the Earth's atmosphere, and Water Cherenkov Detectors which use water tanks detecting the particles produced in the air showers.

3.1 The Fermi Gamma-ray Space Telescope

The Fermi Gamma-ray Space Telecope consists of the Gamma-ray Burst Monitor and the Large Aray Telescope (Fermi-LAT) which are mounted to the Fermi satellite. It has been observing incoming gamma rays from the low Earth orbit since 2008. The Fermi-LAT covers an energy range from 20 MeV to more than 500 GeV and observes the whole night sky with a cadence of 3 h which is accountable to its large field of view. As the telescopes are located in space, their observations entail a very low background in comparison with telescopes located within Earth's atmosphere, however gamma rays in the TeV range cannot be detect as the collection area of the telescope is not large enough. IC 443 observation data provided by Fermi as well as data from its predecessor EGRET are used for the modelling and as a comparison in the course of this study. [21][20][3]

3.2 Imaging Atmospheric Cherenkov Telescopes

Imaging Atmospheric Cherenkov Telescopes (IACT) are used to detect high energy gamma rays within the Earth's atmosphere. They observe the Cherenkov light emitted by the gamma-ray induced atmospheric particle shower.

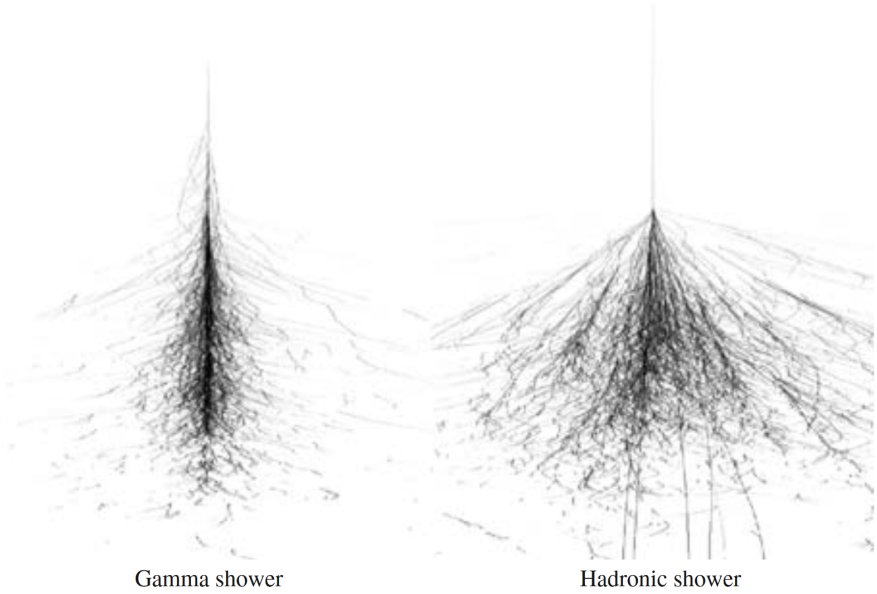

Figure 4: Leptonic (left) and hadronic (right) air showers from Monte Carlo simulations. Note the broader spatial extent of the hadronic air shower as well as the symmetry of the leptonic air shower in first approximation.[22]

Incoming cosmic rays interact with molecules in Earth's atmosphere. This interaction creates different particles, depending on the nature of the incident cosmic ray, which then decay further and produce a cascade of particles (see Figure 4). These air showers are differentiated into electromagnetic and hadronic. Electromagnetic air showers are created by incident high energy gamma rays which produce an electron-positron pair in the atmosphere. These particles then emit new gamma rays through Bremsstrahlung which in turn generate new electron-positron pairs. This process continues until the energy of the final generation of electrons is low enough that ionisation losses become dominant which rapidly cool and decelerate them. Protons and heavier nuclei interact with the atmosphere and produce hadronic air showers, consisting mostly of neutral and charged pions as well as heavier mesons. The former decay into two gamma rays while the latter first decay into muons and then into electrons, positrons and the corresponding neutrinos. Since the particles created within the hadronic air showers posses much more transverse momentum, they are more spatially extended and irregular than their electromagnetic counterpart, as Figure 4 illustrates.

Since the secondary particles travel faster than the speed of light within the atmosphere, they generate Cherenkov light. The peak of the number of air shower particles and therefore Cherenkov light intensity is reached at an altitude of around 10 km. The produced light is beamed around the direction of the incident primary particles and illuminates an area of $\sim 250\,\mathrm{m}$ diameter on the ground which is also called the Cherenkov light pool. For an incident photon with an energy of 1 TeV, only $100\,\mathrm{Photons/m^2}$ of Cherenkov light can be detected on the ground and thus the area covered by an array of IACTs has to be quite large to achieve sufficient photon detection. The hadronic and the electromagnetic air showers create distinctive detection patterns. While the proton showers appear as rather circular and are much more chaotic, the gamma-ray showers appear as a thin ellipse with a clear axis as seen in Figure 5. Therefore images produced by incident gamma rays can be distinguished from those of proton showers. [22][23]

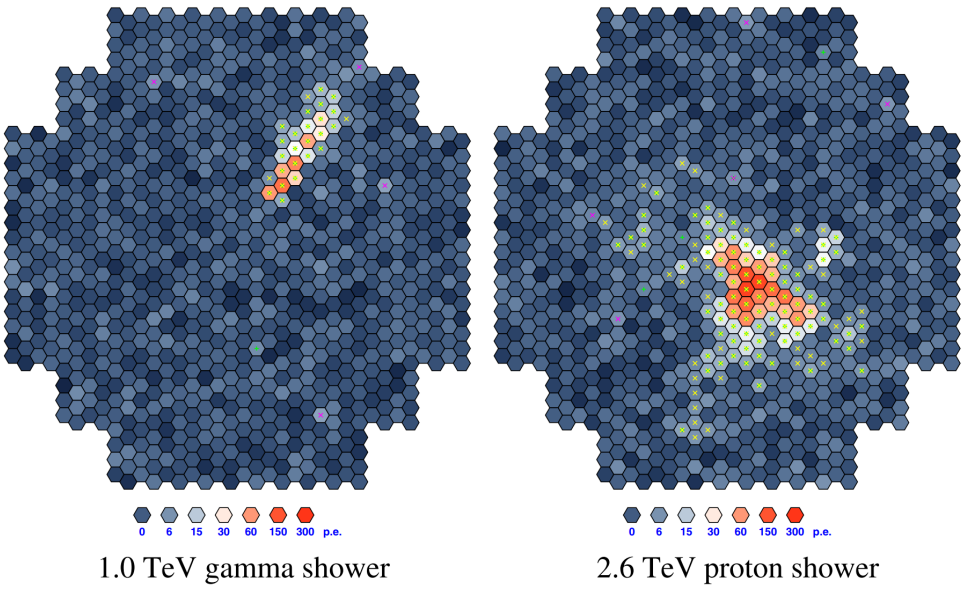

Figure 5: IACT images generated by electromagnetic (left) and hadronic (right) air showers. Note the much broader extent of the proton shower and the clear axis visible in the gamma-ray image. [22]

As seen in Figure 6, images created by the air showers can be described using an ellipse. The geometric properties as well as the location of these ellipses within the image can be described by the so-called Hillas parameters. The width of the ellipse relates to the energy of the incident particle as well as the particle type while the major semi-axis of the ellipse can be used to derive the direction of that particle. For an accurate reproduction of the air shower geometry, multiple IACTs are combined into a telescope array achieving a stereoscopic view of the shower. The direction of the gamma rays can then be reconstructed by combining the images of all telescopes by deriving the intersection of the major semi-axes of the respective ellipses while considering systematic uncertainties (see Figure 6). The Hillas parameters can also be used for particle type and energy reconstruction and therefore a certain part of the hadronic showers can be rejected. However, a substantial background remains in the observations which is handled by the data analysis described in the following sections. [22][23]

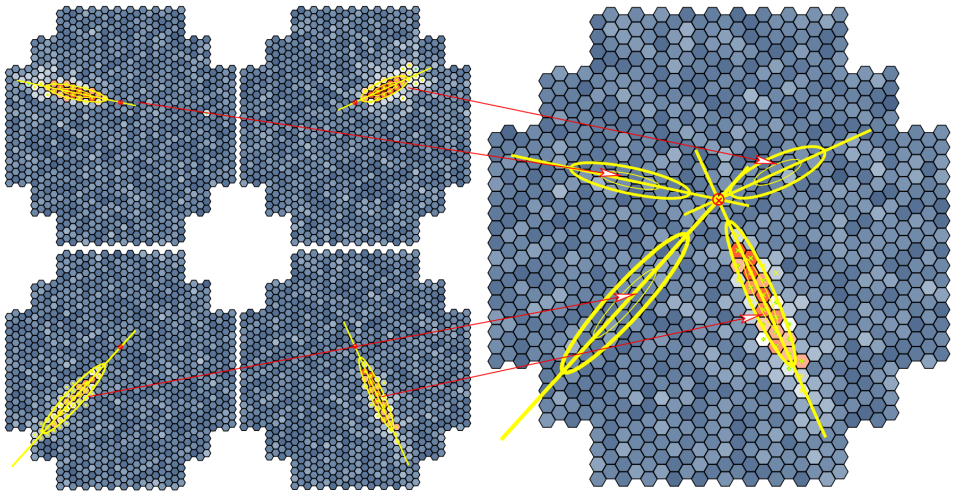

Figure 6: Reconstruction of the Hillas parameters by combining the single telescope images into one image. The intersection is used to obtain the pointing of the incident gamma-ray.[22]

3.3 The High Energy Stereoscopic System

The data which will be analysed in the following sections have been gathered using the High Energy Stereoscopic System (H.E.S.S.) situated at an altitude of 1800 m above sea level in the Khomas highlands in Namibia. Phase I of the telescope array has been operational since December 2003 and it has been upgraded by adding a fifth, larger telescope in phase II of the project in July 2012. Furthermore, the telescope cameras have been upgraded by installing new hardware by 2017 for the initial four telescopes (CT1 to CT4) and the camera of the fifth telescope has been upgraded by 2019.

H.E.S.S. phase I consists of an array of four Imaging Atmospheric Cherenkov Telescopes (IACT) arranged in a square with a side length of 120 m (see Figure 7) with a fifth, larger telescope added to the center of the square in phase II. Each of the phase I telescopes consists of 382 round mirror facets of 60 cm diameter arranged in a sphere of 13 m diameter. This gives each telescope a mirror area of 107 m^2 focusing the incoming light onto the telescope camera sitting at the center of the mirror sphere with a focal length of 15 m. These cameras consist of 960 29 mm, 8 stage photo-multiplier tubes (PMTs) arranged in a hexagonal array. Each PMT covers an area

of 0.16° diameter on the sky adding up to a total field of view of 5°. The telescopes are focused on objects at a distance of 10 km which corresponds to the altitude of the air shower induced Cherenkov radiation.

The triggering system is split into three stages. A single PMT is triggered with a threshold of 4 photo-electrons in an interval of 1.5 nanoseconds. Subsequently, the camera is triggered once a coincidence of 3 pixels within a sector of 8x8 pixels is triggered. Each camera has 38 of these overlapping sectors. Therefore uncorrelated PMT signals produced mostly by the night sky background and other noise is effectively rejected. The data are stored once there is a minimum of two telescope cameras triggered within a frame of 80 nanoseconds. Therefore a stereoscopic view of the air shower is always ensured for all stored events [23].

Furthermore, data from MAGIC and VERITAS which also are IACT arrays will be used. The four VERITAS IACTs have been completed at the Whipple Observatory in souther Arizona in 2007 and have an energy threshold of 300 GeV [5]. MAGIC is a single dish IACT located at 2200 m a.s.l. on the Canary Island La Palma with an energy threshold of 150 GeV [4].

Figure 7: Phase I H.E.S.S. telescopes CT1 to CT4, picture from 2004[4].

[4]https://www.mpi-hd.mpg.de/hfm/HESS/pages/about/pictures/HESS_IMG/index.html

4 Data analysis

4.1 Data Selection

The data analysed in the following sections has been obtained by H.E.S.S. between December 2004 and December 2005 which is during Phase I of the project and therefore only the four telescopes CT1 to CT4 were used for detection. The data have been quality selected analogous to standard H.E.S.S. analysis methods [23]. Therefore data taken under bad atmospheric conditions or system malfunctions are rejected from the further analysis. Furthermore, we require all four telescopes to be operational. The total live-time of the observations after quality cuts amounts to 11.4 hours and was taken using the *wobble mode*, an operation method where the telescopes are pointed to different regions offset from the source allowing for a better background estimation. [23]

4.2 Background Estimation

IACTs not only detect gamma-ray air showers but also those generated by a variety of cosmic rays. These unwanted observations are filtered out using the Hillas parameters (see section 3), however even after this cleaning, some misclassified cosmic-ray events as well as detections of diffuse gamma-ray emissions remain in the data. Hence, before analysing an observation, the observed background needs to be estimated and removed from the data. For this analysis, the background model has been estimated using a spectromorphological model developed from archival H.E.S.S. data, containing no known gamma-ray contamination. This model is added to the *FITS*-files and can be adapted to the respective observation conditions by adjusting its spectral parameters. The observation conditions depend on the atmosphere as well as the instrument response function (IRF) of the IACT array. The IRF can be assumed to be split into three independent components:

$$R(p, E|p_{true}, E_{true}) = A_{eff}(p_{true}, E_{true}) \cdot PSF(p|p_{true}, E_{true}) \cdot E_{disp}(E|p_{true}, E_{true}) \qquad (2)$$

With $A_{eff}(p_{true}, E_{true})$ the effective collection area of the IACTs, $PSF(p|p_{true}, E_{true})$ the point spread function, which is the probability density of an observation of true position and energy (p_{true}, E_{true}) being measured at a position p. $E_{disp}(E|p_{true}, E_{true})$ is the energy dispersion which is the probability to reconstruct the photon energy at energy E when the true energy and position are (p_{true}, E_{true}). The background model as well as the IRF are included in the observation data. [24] [25]

4.3 Gammapy

This analysis is conducted using the up to date version 1.20.0 of Gammapy[5] [24], an open source Python package developed for the evaluation of data from different IACT instruments, Fermi-LAT and HAWC.

The observation data are then projected onto a coordinate system defined by Gammapy's map geometry class WcsGeom with a field of fiew (FoV) of $6° \times 6°$ and a binning of $0.02°$ around the direction of the IC 443 center found by MAGIC (see Table 3, [4]). The energy axis of the map geometry is logarithmically binned in 24 bins in an energy range of $0.1\,\text{TeV} - 100\,\text{TeV}$ while the true energy axis is binned in 48 bins over the same energy range.

[5] https://gammapy.org

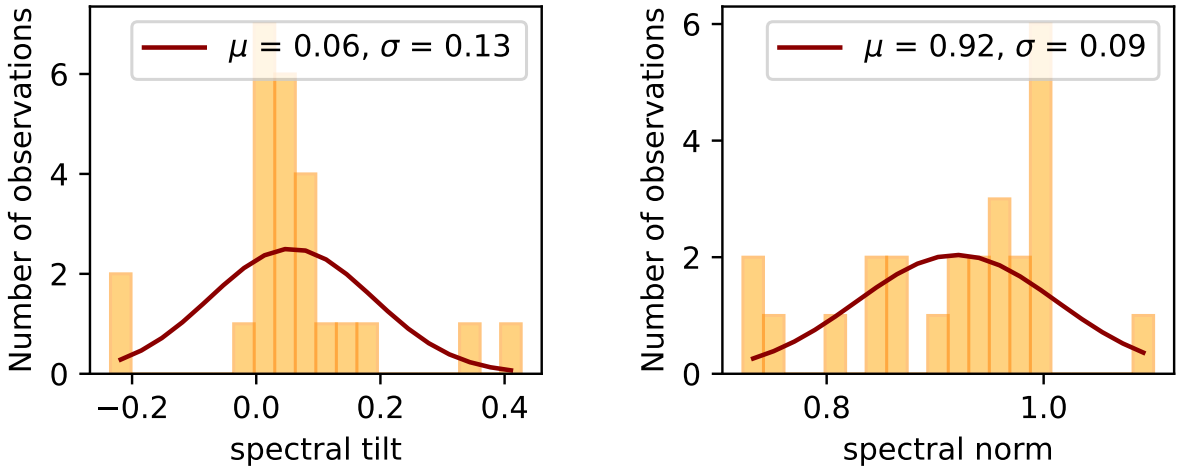

Figure 8: Spectral tilt and norm distribution after quality cuts, masking and background fitting.

The background estimation is then improved by initially taking the location of known sources in the region of the map geometry into account and subsequently defining safe regions for those regions which will be excluded from the further analysis. Furthermore, a region with a FoV of 0.4° around the MAGIC IC 443 center sky coordinates is masked to exclude the source from the background estimation.

In Gammapy, the analysis can either be done in the *stacked* or the *joined* method. While a joint analysis evaluates each run individually and then compiles a resulting maximum likelihood as a product of the individual values, the stacked analysis first sums the counts, background and exposure and averages the PSF and energy dispersion of the individual runs. The stacked data analysis is thus computationally much more efficient while the joined analysis provides more precise results [24]. Before stacking the results, the background is fitted for each run taking spectral tilt and norm as free parameters. Their distribution is expected to be a normal distribution centered around zero for the tilt and around one for the norm. As there is a relatively low number of runs available, the achieved distributions are within an acceptable deviation from the expected values (see Figure 8).

After completing the background estimation, the correlated excess and significance maps are calculated using Gammapy's ExcessMapEstimator class with a correlation radius of 0.16°. Generally, Gammapy contains a variety of estimators using different stochastic methods. The ExcessMapEstimator estimates the significance based on the Li & Ma solution [26]:

$$S_{LM} = \sqrt{2}\left(N_{on}\ln\left(\frac{(1+\alpha)\,N_{on}}{\alpha\,(N_{on}+N_{off})}\right) + N_{off}\ln\left(\frac{(1+\alpha)\,N_{off}}{\alpha\,(N_{on}+N_{off})}\right)\right)^{1/2} \tag{3}$$

With α the ratio of the on-source time t_{on} to the off-source time $t_{off}{}^{t_{on}}/_{t_{off}}$, N_{on} the counts of on-source photons and N_{off} the off-source counts.

This method also called backward folding gives the significance as the excess over the null hypothesis. In first approximation assuming one degree of freedom, the significance can also be given as $\sqrt{\Delta TS}$ which is the unit used in the calculated significance maps. The test statistic value TS is defined using the logarithm of the likelihood $\mathcal{L}$ as $TS = -2\ln(\mathcal{L})$. The difference between two source hypotheses and especially a proposed source model and the null hypothesis

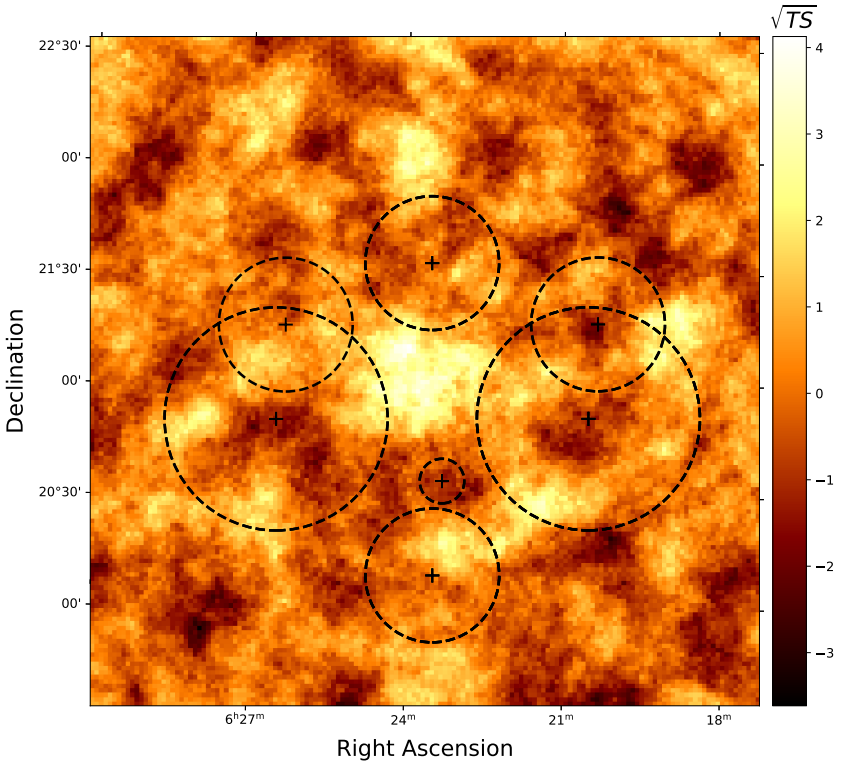

Figure 9: Significance map centered around the IC 443 position determined by MAGIC [4]. The cross markers denote the pointing positions of the individual observations taken by H.E.S.S. while the circle radii indicate the amount of data taken at the respective pointing positions. Note also the excess at the map's center.

can be evaluated by obtainind the difference between the two respective TS values:

$$\Delta TS = TS_{model\,1} - TS_{model,2} = -2\ln\left(\frac{\mathcal{L}_1}{\mathcal{L}_2}\right) \tag{4}$$

This ΔTS is χ^2-distributed for a sufficiently large sample size and is defined to be negative ($-\sqrt{\Delta TS}$) in areas where the background is overestimated. The hypothesis proposed by a source model can be described as the predicted gamma-ray emission of the model not changing the observed emission in the FoV. Thus a model is accepted if the emission is modelled sufficiently well.

The significance and excess maps are projected to a cutout with a FoV of $2.5° \times 2.5°$ around the IC 443 position derived by MAGIC in Figure 9 [4]. Markers indicating the pointing positions and circles with the radius representing the amount of data at the respective positions have been added to the significance map Figure 9. There is a clear emission excess visible in the center of the map, however lower significance emissions at the borders of the source as well as background emissions are also visible which are mainly accountable to the low observation time of 11.4 h after quality cuts and the therefore low significance of the source detection.

4.4 Source fitting and results

To obtain further information about the extent and position as well as the spectral attributes of this source, different models are fitted to the data. The spectral model used in the further analysis is a simple power law of the form:

$$\Phi(E) = \Phi_0 \cdot \left(\frac{E}{E_0}\right)^{-\Gamma} \tag{5}$$

With E_0 the reference energy, Φ_0 the amplitude, Γ the spectral index and E the energy. The reference energy E_0 for this study is set to $E_0 = 1.0\,\mathrm{TeV}$. This choice of the spectral model ensures a low number of degrees of freedom while fitting the spectrum sufficiently well. Furthermore, two different spatial models are fitted and evaluated to obtain the model which best describes the observed emission in the region of IC 443. The fit is performed using the iminuit back end, which is an interactive Python based minimizer implemented in Gammapy [27]. To further assess the fitted model, the significance distribution is visualized in a histogram with a curve fit to the distributions before and after implementing the respective models. A perfect source fit would entirely remove the source and therefore only random noise from the background would contribute to the distribution resulting in a Gaussian with a mean of $\mu = 0$ and a standard deviation of $\sigma = 1$ (see Figure 11).

Gaussian spatial model

The first model used for fitting the observation data is a two dimensional spatial Gaussian which in the usual limit of small sky angular distance to the model center, θ, is of the form:

$$\Phi(lon, lat) = \frac{1}{2\pi\sigma^2} \cdot \exp\left(-\frac{1}{2}\frac{\theta^2}{\sigma^2}\right) \tag{6}$$

Here, σ is the 42% containment radius of the Gaussian and (lon,lat) the center position of the source. The parameters resulting from the iminuit fit can be seen in Table 1. The test statistic values compared to the null hypothesis is $\Delta TS = 26.5$ and the corresponding significance 3.97σ.

type	parameter	value	unit
spatial	R.A. (J2000)	94.39 ± 0.07	deg
spatial	Dec. (J2000)	22.58 ± 0.05	deg
spatial	σ	0.17 ± 0.04	deg
spectral	Φ_0	$(2.5 \pm 0.7) \cdot 10^{-12}$	$TeV/\mathrm{s\,cm^2}$
spectral	Γ	3.5 ± 0.6	

Table 1: Best fit values of the Gaussian model

Disk spatial model

The second spatial model used for source fitting is the disk model. The disk is of the form:

$$\Phi(lon, lat) = \frac{1}{2\pi(1 - \cos r_0)} \cdot \begin{cases} 1 & \text{for } \theta \leq \mathrm{r_0} \\ 0 & \text{for } \theta > \mathrm{r_0} \end{cases}, \tag{7}$$

With θ the sky separation, r_0 the radius of the disk and (lon, lat) the position. The edge of the disk is smoothed using an error function with an edge width α as the boundary for better fitting of the model. r_0 is defined to be at 50% of the height of the disk and therefore at $0.5 \times \alpha$. For the disk model, the resulting test statistic value in relation to the null hypothesis is $\Delta TS = 27.9$ which translates to a significance of 4.12σ.

type	parameter	value	unit
spatial	R.A. (J2000)	94.36 ± 0.04	deg
spatial	Dec. (J2000)	22.56 ± 0.03	deg
spatial	r_0	0.29 ± 0.03	deg
spectral	Φ_0	$(2.3 \pm 0.5) \cdot 10^{-12}$	$TeV/s\,cm^2$
spectral	Γ	3.5 ± 0.5	

Table 2: Best fit values of the disk model

Model comparison

For better comparison, the extension of both spatial models is plotted on the significance and excess map computed before the source model is fitted to the data. There, the similarity in position and extension is clearly visible (see Figure 10). Note however that the radius of both models contain slightly different amount of counts. While the extension of the Gaussian model is the 68% containment radius, the extension of the disk model is a circle of disk radius r_0.

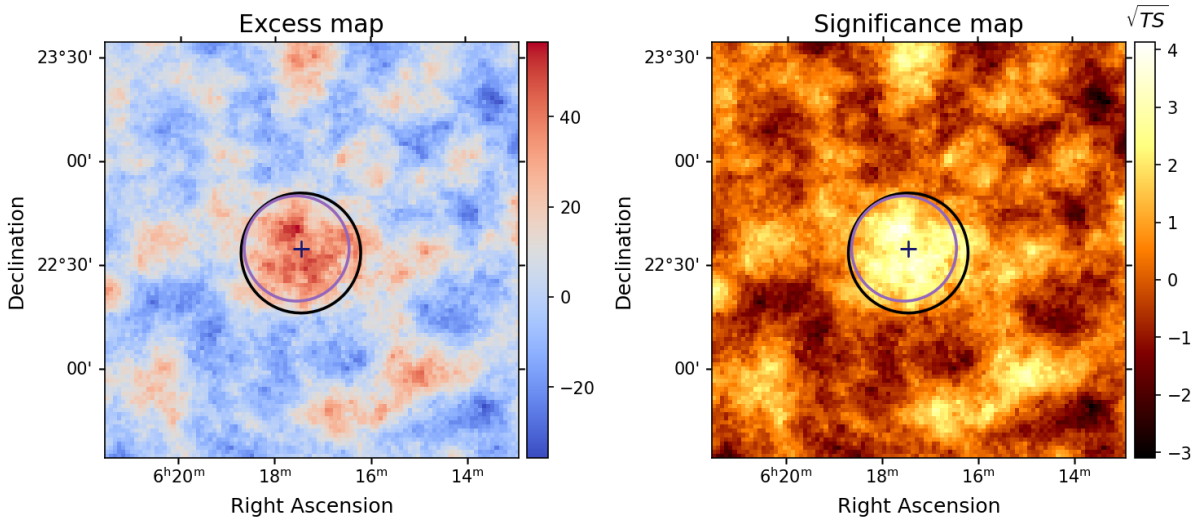

Figure 10: Significance and excess maps before fitting with the outline of the gaussian model in lilac and the outline of the disk model in black. The radius of the Gaussian model is $\theta^{ext}_{68\%}$ while the radius of the disk model is r_0. The cross marker denotes the fitted center position of the disk model (see Table 2)

For further comparison, significance distribution histograms are examined (see Figure 11). The fit of both histograms are quite similar as both fitted models describe the source almost equally well. The medians $\mu = 0.02$ and $\mu = 0.03$ are almost at the optimal value of $\mu = 0.0$ and the excess significance $\sigma = 0.89$ is also sufficiently close to the optimal value of $\sigma = 1$. With

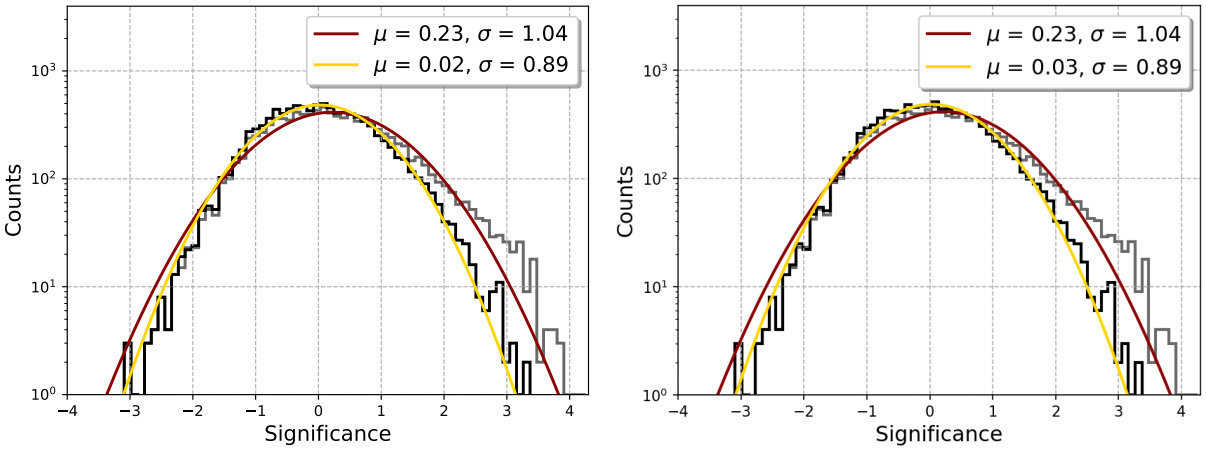

(a) (b)

Figure 11: Significance distribution histogram for the fit of the Gaussian (a) and the Disk (b) spatial models. The red line is a fit of the histogram before the spatial model is fitted, while the yellow line is after model fitting and removing the fitted source. μ and σ of both models are sufficiently close to the optimal values of $\mu = 0$ and $\sigma = 1$ for perfect source fitting.

these results it becomes clear that both models are a good fit to the source and they are almost indistinguishably close in their significance distributions. The quality of the fit can further be assessed by comparing the test statistic value and the corresponding significance over the null hypothesis of both models. As the significance of the disk model 4.12σ is higher than that of the Gaussian model 3.97σ, the disk model is preferred and used in the further analysis.

Comparison with literature values

Model	R.A. (°)	Dec. (°)	Extension (°)
Disk	$94.36 \pm 0.04 \pm 0.006_{sys}$	$22.56 \pm 0.03 \pm 0.006_{sys}$	$r_0 = 0.29 \pm 0.03 \pm 0.006_{sys}$
Gaussian	$94.39 \pm 0.07 \pm 0.006_{sys}$	$22.58 \pm 0.05 \pm 0.006_{sys}$	$\theta^{ext}_{68\%} = 0.25 \pm 0.05 \pm 0.006_{sys}$
MAGIC	94.17 ± 0.04	22.53 ± 0.04	$\theta^{PSF}_{68\%} = 0.1 \pm 0.01$
VERITAS	94.21 ± 0.11	22.51 ± 0.11	$\theta^{ext}_{68\%} = 0.24 \pm 0.11$
Fermi	94.31 ± 0.03	22.58 ± 0.03	$\theta^{ext}_{68\%} = 0.27 \pm 0.04$

Table 3: Summary of locations and extensions of the best-fit results derived by different experiments.

For better understanding of the quality of the results, they are compared to IC 443 observations by MAGIC [4], VERITAS [5], and the Fermi-LAT [20]. The characteristics obtained by the other experiments as well as those of this study can be seen in Table 3. Furthermore, the extensions of IC 443 as determined by the fit of disk and gaussian models to H.E.S.S. data, compared to the results by MAGIC, VERITAS and Fermi-LAT are plotted on significance and excess maps derived from the H.E.S.S. data with a smaller $1° \times 1°$ FoV for better visibility of the difference between the individual results as shown in Figure 12.

In Figure 13, the uncertainties of the radius and position are presented for better comparison. The systematic pointing uncertainties of H.E.S.S. are 20“ per axis and is mainly caused by slight

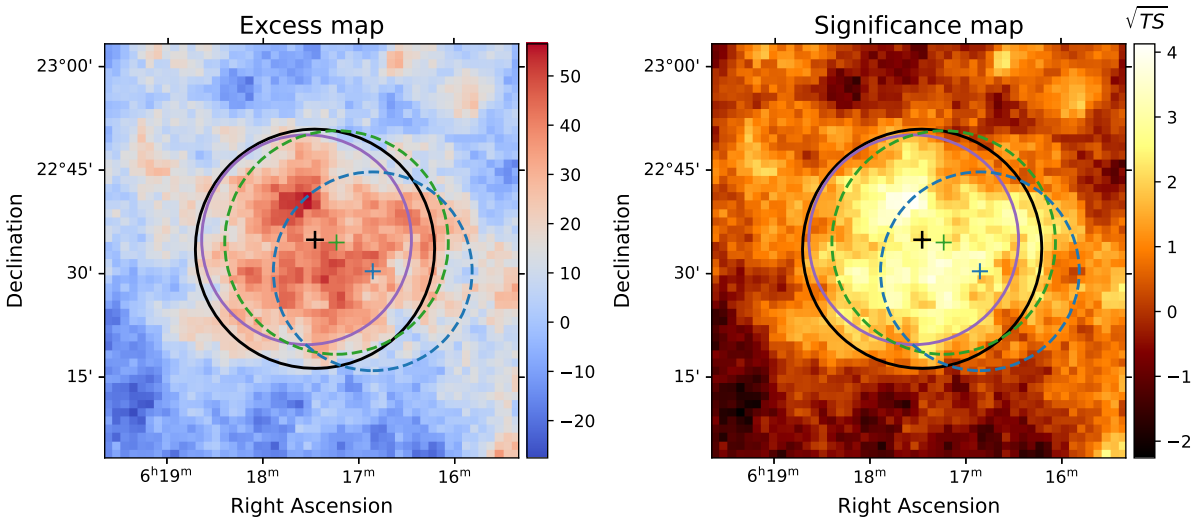

Figure 12: Excess and significance maps with a smaller $1° \times 1°$ FoV. The center positions are denoted by cross markers in green for Fermi-LAT [20], blue for VERITAS [5] and black for the disk model. The extensions are marked as circles with a radius of $\theta_{68\%}^{ext}$ for the Gaussian model (purple), Fermi-LAT [20] (green) and VERITAS [5] (blue). The black circle indicates the extension with r_0 of the disk model.

fluctuations in the steel telescope mounts [1]. It is included in Table 3 and in Figure 13. The extension and the center position of IC 443 derived by the models of this study are closest to the Fermi-LAT results [20] while the center positions of VERITAS [5] and MAGIC [4] are slightly shifted. Within errors, the results derived by the analysis of VERITAS data are still compatible with the H.E.S.S. results as the uncertainties stated by VERITAS are comparatively large. The MAGIC IC 443 position is within 3σ of the Disk and Gaussian positions. The extensions derived by the different models are also quite similar. MAGIC assumes a point source and therefore the extension visualized in Figure 13 is the 68% containment radius and the corresponding error of the PSF $\theta_{68\%}^{PSF} = 0.1 \pm 0.01°$ [20][5][4].

Spectral energy distribution

For spectral considerations, the spectral energy distributions (SED) is computed visualizing the fit of the power law spectral model conducted by iminuit which obtained a flux normalization of $\Phi_0 = (2.3 \pm 0.5) \cdot 10^{-12}\,\mathrm{TeV/cm\,s^2}$ and a spectral index $\Gamma = 3.5 \pm 0.5$ for the best fitting disk model (see Table 6, Table 5). The so-called flux points of the SED are estimated using Gammapy's FluxPointsEstimator class with six logarithmically spaced bins over an energy range of $0.1\,\mathrm{TeV} - 100\,\mathrm{TeV}$. The estimator selects the closest to the requested energy edges from the parent dataset (24 bins over the range $0.1\,\mathrm{TeV} - 100\,\mathrm{TeV}$) and refits the index and amplitude of the best fit model in every energy bin. Additionally to the flux points, the power law spectral model with its corresponding error are plotted given the fitted parameters seen in Table 2. The flux axis is multiplied with the square of the energy for better visibility. The estimator gives upper limits for flux points with 2σ [24]. The choice of rather large bins is accountable to the low observation time and therefore low accuracy of the spectral data. A more detailed spectral analysis as well as a discussion of the results is conducted in the following sections.

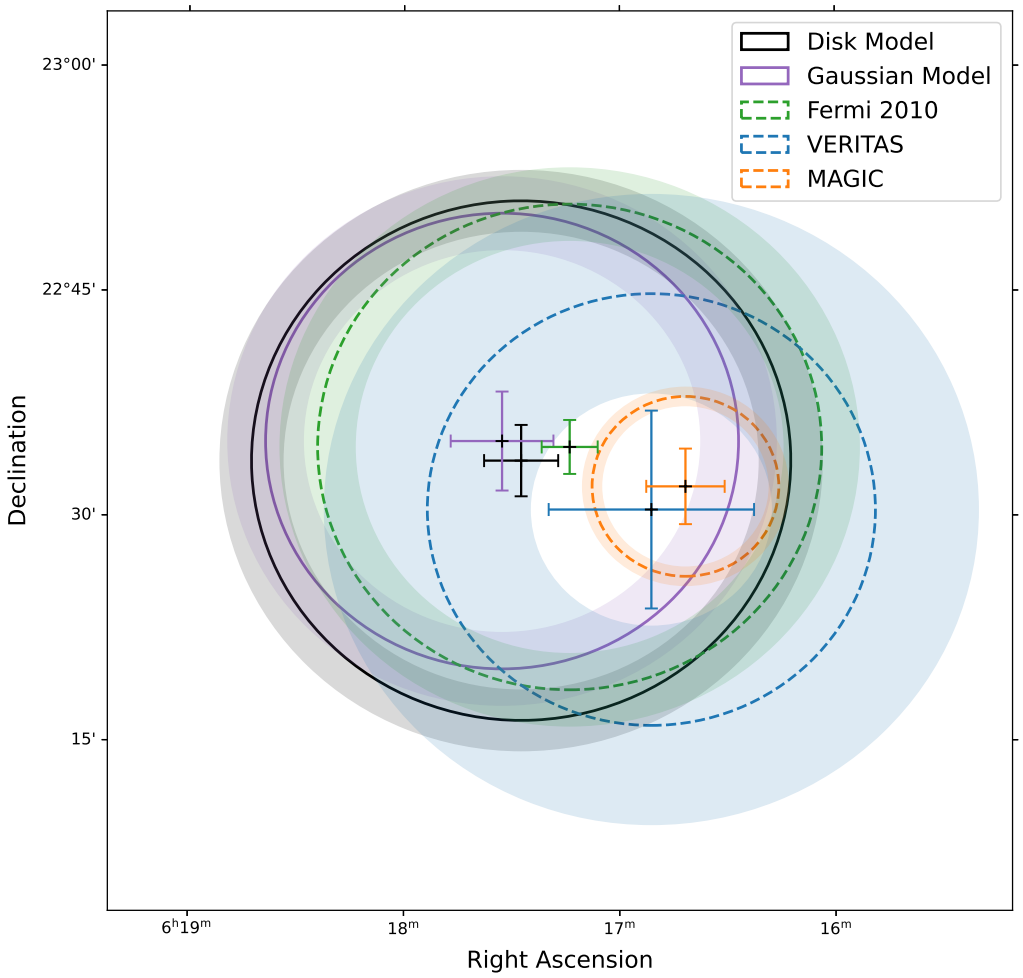

Figure 13: Comparison of IC 443 positions, extensions, and their respective uncertainties of literature values as well as the two fitted models. The plotted uncertainties are the sum of statistic and systematic uncertainties stated in Table 3. The radius uncertainties are shown as a shaded band around the respective model outlines. Note that MAGIC models IC 443 as a point source and therefore the extension is the $\theta^{PSF}_{68\%}$ of the PSF [4].

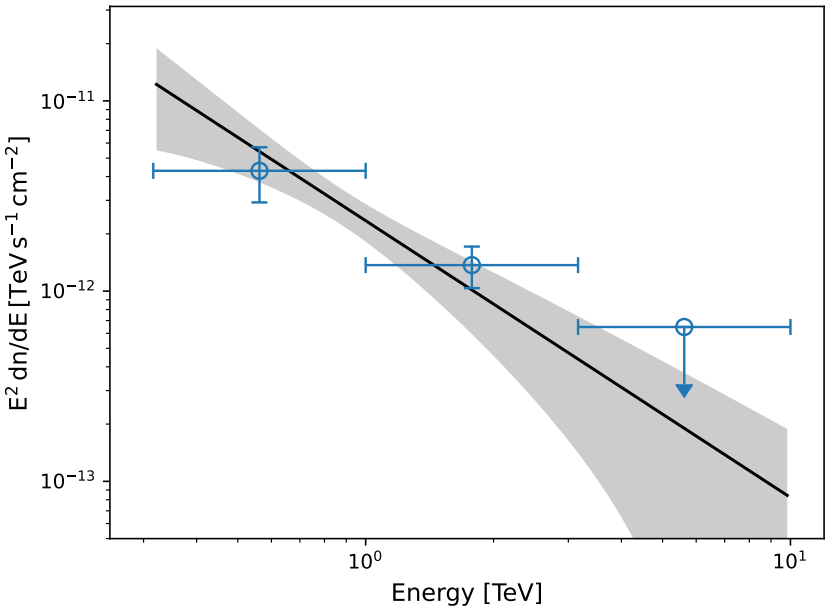

Figure 14: Spectral energy distribution of the power-law spectral model. The flux axis is multiplied with E^2 for better visibility.

5 Physical modelling and Discussion

For better understanding of the physical processes leading to the gamma-ray emission observed from IC 443, physical modelling to the observed spectrum is conducted. This modelling aids in distinguishing between the emission created from the different parent particle populations described in section 2.2. The main two subgroups of gamma-ray emission mechanisms are based on hadronic or leptonic particle populations which create different characteristic spectra in the gamma-ray observations. To fully understand the observed emission, a larger energy range than covered in the H.E.S.S. observations needs to be analysed as both the pion decay gamma-ray emission as well as leptonic interactions are mostly located at lower energies. Therefore, especially the detection by the Fermi-LAT [20] needs to be considered as its energy range covers this low-energy range (see section 5.3).

5.1 Naima

A physical model is derived using version 0.10.0 of the *naima*[6] [28] Python package which is developed for modelling and fitting an observed gamma-ray emission from an underlying particle population. The package is split into two main sections, a set of radiative models and a set of utility functions. In the naima version used in this analysis, the radiative models of synchrotron, inverse Compton, non-thermal bremsstrahlung and neutral pion decay as well as the option of defining custom models are available. The spectral energy distribution resulting from the gamma-ray production of one of these models can be fitted with a set of utility functions based on Markov Chain Monte Carle (MCMC) sampling. The fit quality can then be assessed by reviewing the respective likelihood and uncertainty values. Naima implements the emcee[7] package as an algortihm for MCMC sampling. [29]

Radiative Models

In the further analysis a relativistic proton particle population with neutral pion decay as the gamma-ray production mechanism is assumed. The pion decay class uses the parameterization provided by [30] and takes information about the underlying particle distribution as well as the density of the emission region n_H which is assumed to be $n_H = 20\,\mathrm{cm}^{-3}$ as stated by the 2013 Fermi-LAT analysis [3]. The evaluated proton distributions are a simple power law for the modelling of only the H.E.S.S. flux points while a power law with exponential cutoff as well as broken power law are used for studying the combined spectral model of the before mentioned gamma-ray observations.

The power law distribution provided by naima is of the shape:

$$f(E) = A \left(\frac{E}{E_0} \right)^{-\alpha}, \tag{8}$$

with the proton energy E, the reference energy E_0, an amplitude A and a spectral index α (similar to Equation 5). The broken power law class provided by naima is parameterized by:

$$f(E) = \begin{cases} A \left({}^{E}/_{E_0} \right)^{-\alpha_1} & : E < E_{break} \\ A \left({}^{E_{break}}/_{{E_0}^{\alpha_2 - \alpha_1}} \right) \left({}^{E}/_{E_0} \right)^{-\alpha_2} & : E > E_{break} \end{cases}, \tag{9}$$

[6] https://naima.readthedocs.io/
[7] https://emcee.readthedocs.io/

with E_{break} the break energy and the two spectral indices α_1 and α_2. Furthermore naima's exponential cutoff power law can be described by:

$$f(E) = A\,(E/E_0)^{-\alpha} \exp\left(-\,(E/E_{cutoff})^{\beta}\right), \tag{10}$$

with the exponential cutoff energy E_{cutoff} and the cutoff exponent β.

The fitted observation data computed in the sections before as well as the particle distribution functions and the gas density of the emission region is taken by the respective radiative models and a spectrum is simulated for a parameter vector. This vector is made of the parameters taken by the particle distribution function and gives the starting values for the further fitting process. The radiative model class then calculates a spectral energy distribution as well as the energy distribution of the parent proton population.

Markov Chain Monte Carlo sampling

The MCMC sampling is implemented into naima by using the emcee Python package. Naima assumes the observed spectral data and the corresponding errors to be correct, Gaussian and independent which is not the case for most data and may be solved by future versions of naima. For a set of parameters $\vec{p}$ with the spectral model $S(\vec{p}, E_i)$ the logarithm of the likelihood can be written as:

$$\ln \mathcal{L} \propto -\frac{1}{2} \sum_{i=1}^{N} \frac{\left(S\left(\vec{p}, E_i\right) - F_i\right)^2}{\sigma_i^2} \tag{11}$$

with (F_i, σ_i) the flux measurements and uncertainty at the energy E_i over N spectral measurements. This equation disregards constant terms as the MCMC sampler only deals with differences in the logarithm of the likelihood which eliminate these terms. The log-likelihood expressed in Equation 11 can be related to χ^2 by $\chi^2 = -2 \ln \mathcal{L}$ and therefore a maximization of the log-likelihood is desirable. In the optimization process, prior likelihood parameters are passed to the MCMC sampler providing information about our knowledge of the value and range of the respective parameters. This provides the user with a handle to increase the efficiency as well as the accuracy of the optimization.

The fitting process is handled by naima's sampler class and takes a parameter vector as the starting position. This vector is then fitted to the observed spectrum by a number of walkers and steps which can be defined by the user. Increasing the number of simultaneous walkers improves the efficiency of the MCMC sampling process as it decreases the number of likelihood calls which are taken to assess the fit of the current parameters. The steps of the fitting process are saved in chains which denote the values the respective walkers take while a certain number of steps are discarded from the chain to reduce the influence of the starting position of the walkers. Furthermore, the best fit values with the corresponding uncertainties as well as the logarithm of the maximum likelihood is stored. [28]

5.2 Modelling of the H.E.S.S. data

First, the H.E.S.S. flux points obtained in the previous analysis steps are modelled by utilizing naima's power law function as the particle distribution. The observed gamma-ray spectrum directly mirrors this particle distribution and thus the H.E.S.S. flux points can also be modelled by this function as done by the previous gammapy analysis (see Figure 14). For the purpose of limiting the degrees of freedom of the fitted function, the reference energy is frozen to $E_0 = 1\,\mathrm{TeV}$

$A\ [\mathrm{TeV}^{-1}]$	α	E_0 [TeV]	$\ln(\mathcal{L})$	χ^2/dof
$8^{+3.1}_{-2.3} \times 10^{47}$	$3.0^{+0.13}_{-0.14}$	1	-0.35	$0.7/1$

Table 4: Best fitting proton spectrum and fit quality parameters of the H.E.S.S. flux points

and will therefore not be fitted by the MCMC process. The sampling procedure is run with 256 simultaneous walkers (chains), 100 steps of *burn-in* and 150 steps of *run*.

The quality of the fitted model can be assessed by reviewing the resulting log-likelihood values and thus inferring the corresponding reduced chi-squared value χ^2/dof. Here, dof are the degrees of freedom which in the context of fitting the spectral model to the flux points is the difference between the number of points and the free parameters of the fitted function ($dof = 1$ for the H.E.S.S. model). The resulting reduced chi-squared value for the H.E.S.S. flux points is $\chi^2/dof = 0.69/1$. The best fitting parameters as well as the respective uncertainties can be seen in Table 4 whereas the amplitude is given as the normalization of the particle distribution at 5 TeV.

Furthermore, the SED with the spectrum of the maximum likelihood model as a black line and the other sampled spectra as gray lines is shown in Figure 15. The lower panel of the figure shows the deviation of the flux points from the fitted spectrum in $\Delta\sigma$. The corresponding energy distribution of the proton population is shown as an inset. [28]

5.3 Multi wavelength modelling

To obtain an emission model covering a more representative energy range, the combined SED using results from Fermi-LAT [20], MAGIC [4], VERITAS [5], and H.E.S.S. is considered. The shape of the SED can best be described by either a power law function with exponential cutoff (see Equation 10) or a broken power law function (see Equation 9) and thus these functions will be used as the particle distribution in the naima modelling procedure. The 36 combined flux points are modelled by the functions with five parameters and thus the resulting degrees of freedom are $dof = 31$. For both particle distributions, the MCMC sampling process is run by 256 walkers in 100 *burn-in* and 150 *run* steps. The resulting parameters and fit quality parameters can be seen in Table 5 and Table 6.

$\log_{10}(A)$	α	E_0 [TeV]	β	E_{cutoff} [TeV]	$\ln(\mathcal{L})$	χ^2/dof
$44.9^{+0.5}_{-0.6}$	$1.6^{+0.3}_{-0.2}$	$163^{+7.5}_{-7.1}$	$0.54^{+0.05}_{-0.04}$	$0.31^{+0.03}_{-0.03}$	-48.3	$96.6/31$

Table 5: Best fit and fit quality parameters of the power law function with exponential cutoff as the particle distribution with the amplitude A in TeV^{-1}. Parameter names from Equation 10.

$\log_{10}(A)$	α_1	E_0 [TeV]	α_2	E_{break} [TeV]	$\ln(\mathcal{L})$	χ^2/dof
$46.4^{+0.5}_{-0.5}$	$2.31^{+0.02}_{-0.02}$	$6^{+4.0}_{-2.4}$	$3.13^{+0.02}_{-0.02}$	$0.15^{+0.06}_{-0.06}$	-36.5	$73/31$

Table 6: Best fit and fit quality parameters of the broken power law function as the particle distribution with the amplitude A in TeV^{-1}. Parameter names from Equation 10.

Furthermore, the walkers (chains) can be analysed by a set of diagnostic plots provided by

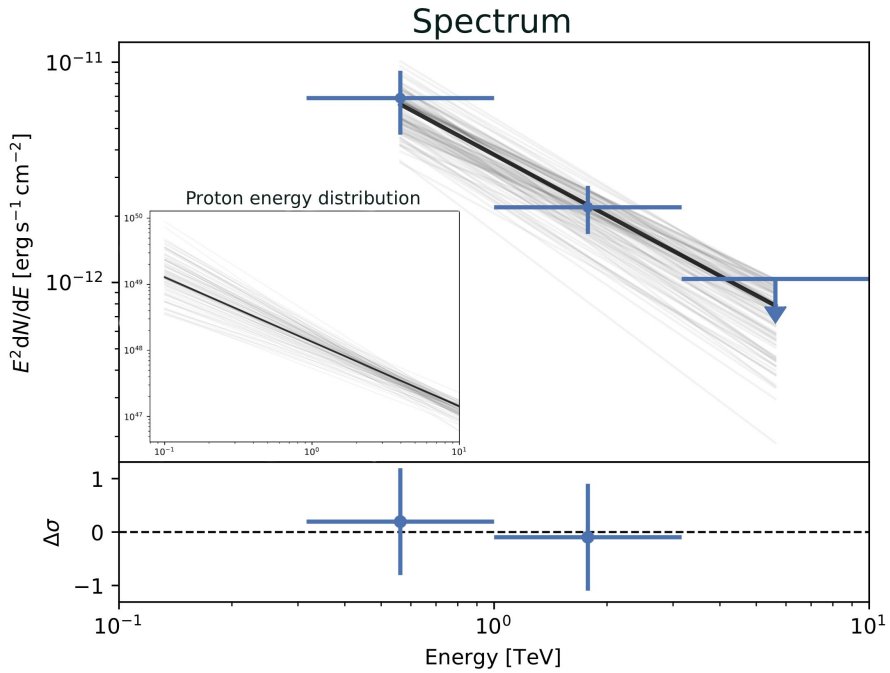

Figure 15: Spectral energy distribution of the power law fit to the H.E.S.S. flux points. The black line visualizes the best fit parameters while the gray lines represent the respective sampled parameters. The lower part of the fits shows the difference of the flux points from the fitted function in measures of standard deviations σ. The inlay shows the proton spectrum simulated from the fitted spectrum, again with the best fit parameters in black and the gray lines representing the sampled values. Here, the energy distribution of the proton population is plotted in erg versus the proton energy in TeV. [28]

naima's plotting functions. The *corner plots* visualize the sampling process and the quality of the fit by showing the distributions of the sampled parameters and scatter plots of parameter pairs. Thereby the range provided to the prior distributions can be assessed and eventual covariances between any two parameters can be seen as they would elongate the shape of the respective scatter plots. This can be seen in Figure 18 as there is a correlation between E_0 and *norm* and no covariance between the other parameters becomes evident. This only holds for pairs of Gaussian distributed priors as uniform distributions produce more rectangular shapes in the scatter plots (see Figure 18, E_{cutoff}).

The resulting combined energy distributions can be seen in Figure 16 for the power law distribution with exponential cutoff as the particle distribution and in Figure 17 for the broken power law distribution. Again, the inset panel shows the corresponding proton energy distribution which is closely related to the observed gamma-ray spectrum. The proton energy distribution of Figure 17 shows a kink at $E = E_{break}$ while that of Figure 16 falls smoothly at high energies. In both cases, the resulting spectra follow the SED closely in the lower energy regimes of the Fermi-LAT data, while Figure 16 shows larger deviations from the observed spectrum in the higher energy range ($E \sim 5\,\mathrm{TeV}$)). The broken power law on the other hand follows the SED more closely in this energy range which is directly mirrored by its lower reduced chi-squared value (see Table 6). The relatively high reduced chi-squared values can be explained by the large

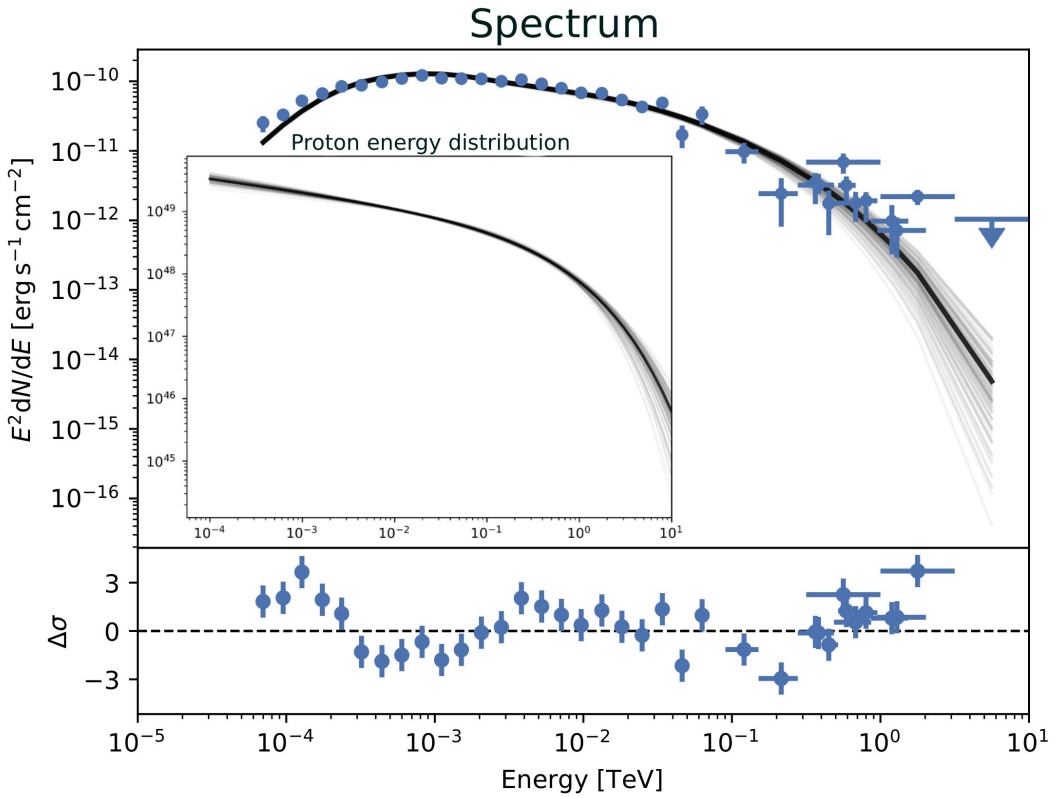

Figure 16: Spectral energy distribution of the fit with a power law with an exponential cutoff as the particle distribution. The fitted SED is given by Fermi [3], MAGIC [4], VERITAS [5] and the H.E.S.S. analysis conducted in the previous sections. The black lines represent the set of best fit parameters while the gray lines are the sampled parameters. Note that the inlaid Proton energy distribution follows the same shape as the SED in the mid- and high-energy range. [28]

scattering of the SED in the higher energy range. Furthermore, the amount of data-points at higher energies is large enough for fitting a sensible curve but not for taking averages of scattered points. Therefore the broken power law function is the preferred model of the proton energy distribution.

For better visualization of the different groups of flux points and the respective errors, the best fit naima model is added to a combined SED. When comparing the H.E.S.S. data with that of the other IACTs (MAGIC [4] and VERITAS [5]), it is evident that the flux obtained from the analysis of the H.E.S.S. data is higher than the flux obtained from the other IACTs (see Figure 19). Furthermore, the VERITAS and MAGIC flux points each cover smaller energy ranges but on average have larger flux errors. As these statistical fluctuations are mainly caused by the analysis technique, the lower errors of the H.E.S.S. data-points can be accounted to the newer analysis procedure using Gammapy which fits the spectrum and morphology of the source at the same time. This was not possible at the release time of the respective MAGIC and VERITAS papers.

Furthermore, when comparing the resulting spectrum (Figure 19 to the expected spectra of the different emission models (Figure 1), the similarity of the observed spectrum with that

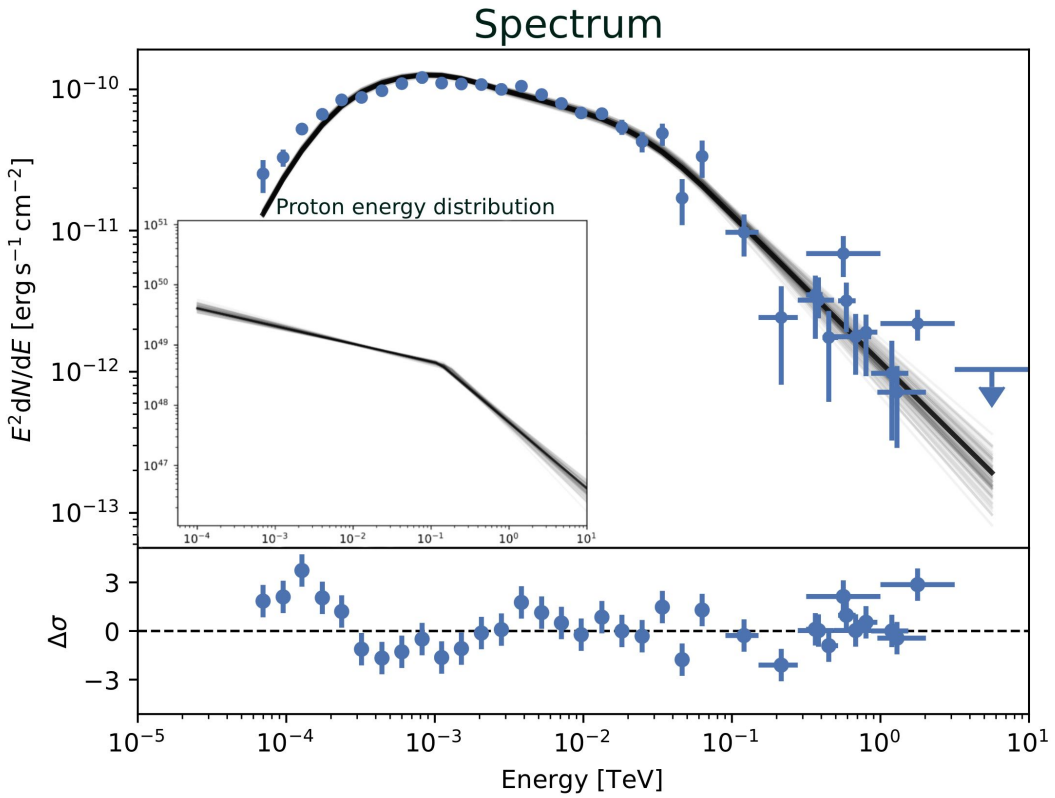

Figure 17: Spectral energy distribution of a broken power law particle distribution fit to the combined SED from Fermi [3], MAGIC [4], VERITAS [5] and the H.E.S.S. points derived in the previous sections. The inlaid figure shows the corresponding Proton energy distribution with a kink at the break energy E_{break}. Note also the lower deviation of the SED from the fitted model comparing to the fit of the power law with exponential cutoff. [28]

resulting from the neutral pion decay gamma-ray production mechanism becomes apparent. Especially the steep gradient of the pion bump at energies of $E \sim 10^{-4} - 10^{-3}$ TeV can be observed which was also stated by [3]. The alternative gamma-ray production mechanisms of purely leptonic emission from inverse Compton scattering and bremsstrahlung are rejected on energetic grounds and issues with fitting the spectrum respectively. The seed photon populations are not large enough to explain the observed gamma-ray spectrum, making inverse Compton scattering implausible. The bremsstrahlung models do not fit the observed spectrum unless an ad-hoc break is introduced which can not be seen in radio emissions when assuming the same electron population are responsible for this spectrum [3]. The maximum energy is reached at $E \sim 10^{-3}$ TeV which is similar to Figure 1 with $\alpha = 2.25$. The change in spectral index of the observed spectrum towards higher energies also closely resembles the expected shape of the neutral pion-decay production mechanism presented by [12]. A similar broken power law spectrum is also reported in the 2013 analysis of Fermi-LAT data which finds $\alpha_1 = 2.35 \pm 0.02$, $\alpha_2 = 3.1 \pm 0.1$ and $E_{break} = 239 \pm 74$ GeV. The break energy obtained by this analysis $E_{break} = 150^{+62}_{-57}$ GeV is lower than that obtained by Fermi-LAT but within errors. Thus the addition of the H.E.S.S. flux points further confirm the characteristic pion-decay spectrum and the presence of a parent population

of relativistic protons is evident. However, the other gamma-ray production mechanisms may still contribute to the observed spectrum at a lower level. [12][28][3]

The observed parent proton population creating pions in collisions with protons and nuclei of the surrounding matter represent a clear characteristic of an SNR interacting with a molecular cloud. Thus the observed spectrum supports the theories derived from 21 cm line emissions as well as the 2013 Fermi-LAT observations. [3][2]

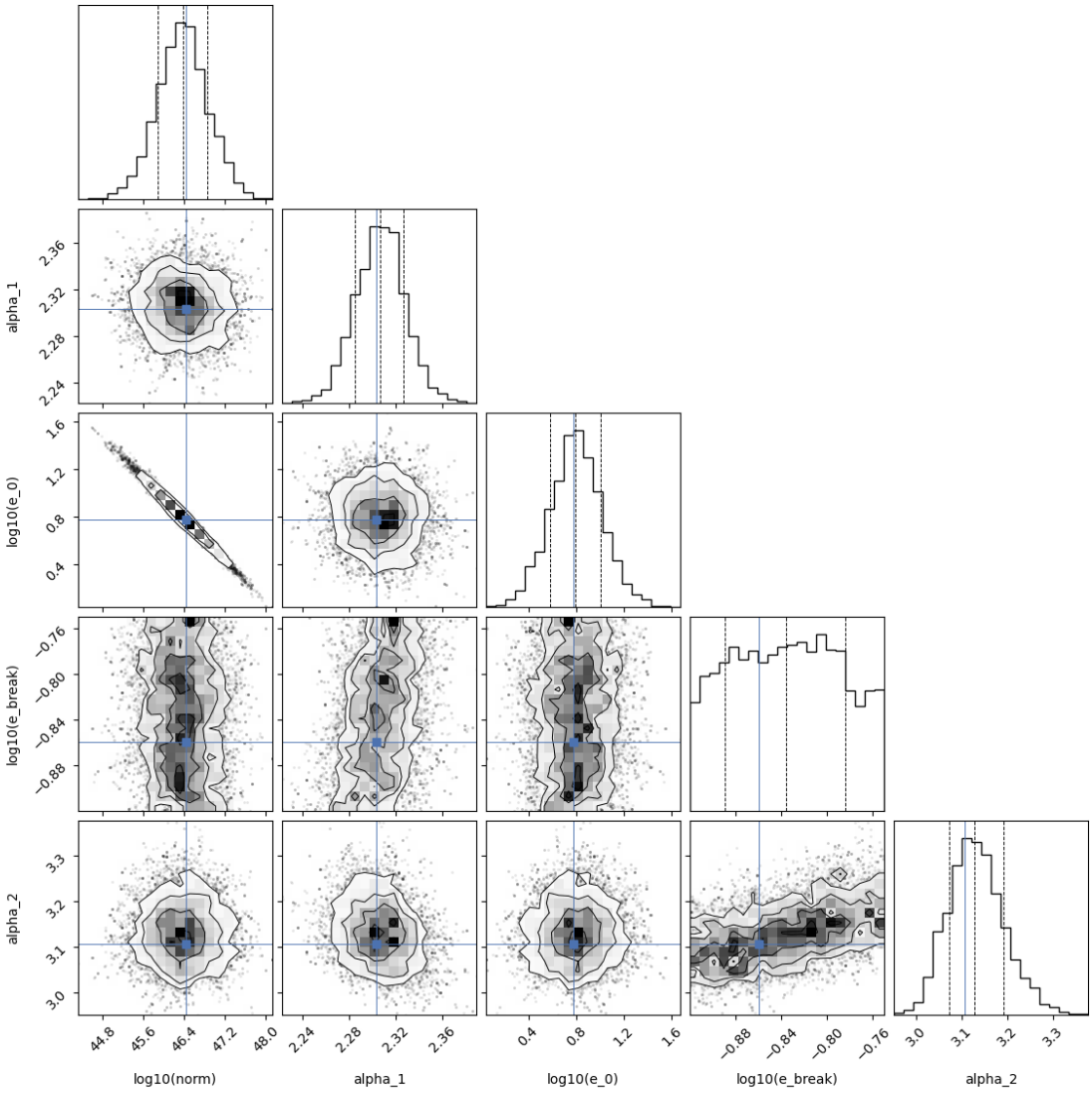

Figure 18: Corner plot of the fit of a broken power law particle distribution. The distributions of all free particles as well as the best fit parameter vector, indicated by the blue crosses are plotted. Note the Gaussian distributions of all parameters except E_{break}. The prior of E_{break} follows a uniform distribution while the others follow a normal distribution. Furthermore, the shape of the norm versus E_0 plot hints to a high covariance. The vertical dashed lines shown in the distribution histograms visualize the respective parameter edges given to the prior distributions. [28]

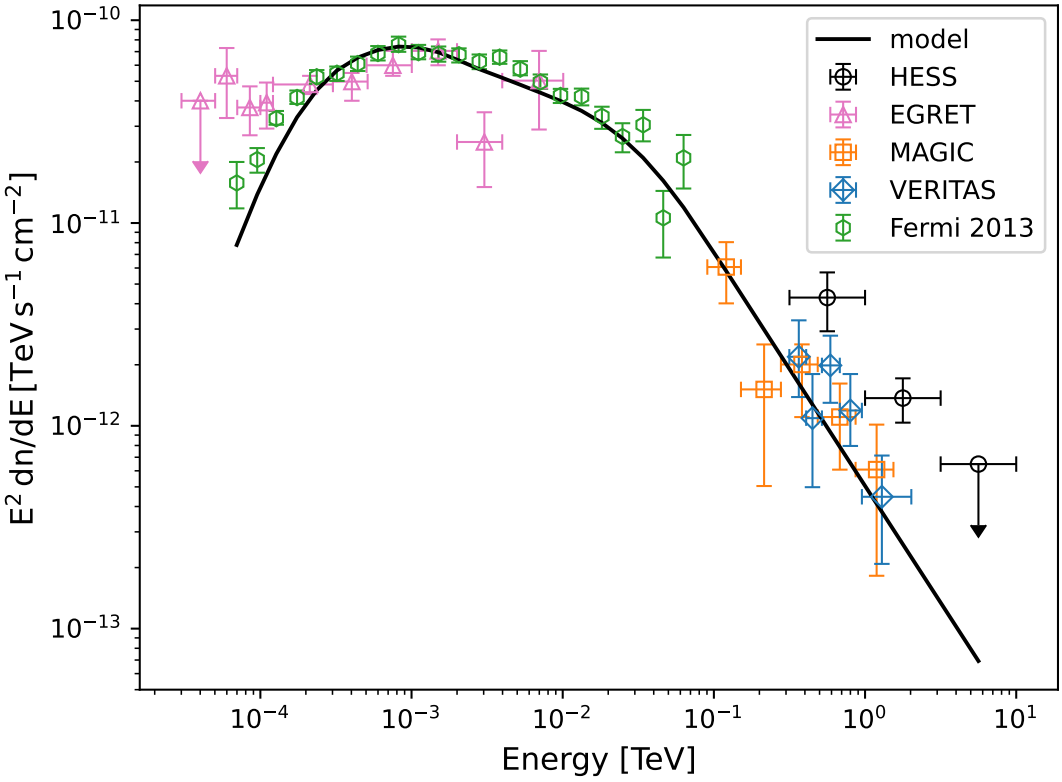

Figure 19: Combined spectral energy distribution with flux points from this H.E.S.S. analysis, Fermi-LAT [3], MAGIC [4], VERITAS [5] and EGRET [19]. The EGRET flux points have not been in the naima modelling process since points from Fermi-LAT, the improved successive project are available. The flux axis has been multiplied with the squared energy for better visualization and the model line is the best fit broken power law model resulting from the previous naima analysis. [28] Note the steep slope in the low energy regime until $\sim 400\,\mathrm{MeV}$ which is characteristic for the pion-bump. [12]

6 Conclusion and Outlook

This work presents a first analysis of high energy gamma-ray observation data of the IC 443 supernova remnant taken by the H.E.S.S. telescope array from 2004 to 2006. After excluding low quality data, likelihood modelling of the spatial and spectral parameters was performed in the energy range of 0.3 TeV-100 TeV. This study finds that the emission can be described best by a disk model centered at R.A.= $94.36° \pm 0.5°$, Dec.= $22.56° \pm 0.04°$ with an extension of $r_0 = 0.29° \pm 0.04°$ and a simple power law model with spectral index $\Gamma = 3.5 \pm 0.5$ and flux normalization $\Phi_0 = (2.3 \pm 0.5) \cdot 10^{-12} {}^{\mathrm{TeV}}/_{\mathrm{s\,cm^2}}$. From this process, a significant observation of an extended source around the IC 443 location could be obtained which is consistent with that of other gamma-ray analyses. The results obtained in this study were then compared to results obtained from other IACTs, and a general agreement is found. Furthermore, a multi-wavelength comparison to the morphologies of X-ray and radio observations to the derived model was conducted to provide further context. After the spatial analysis, flux points fitted by a power law spectral model were computed over an energy range 0.1 TeV-100 TeV.

Additionally, physical modelling of the gamma-ray production was conducted while assuming a parent proton population producing gamma rays through the pion-decay mechanism. The energy distribution of this proton population was modelled by a power law for the H.E.S.S. flux points. To obtain a more representative energy range, the flux points from other IC 443 gamma-ray observations were considered. These were modelled by a broken power law and a power law with exponential cutoff as the particle distributions. The fit quality of these models was then assessed by evaluating the respective reduced chi-squared values, which leads to the selection of the broken power law fit as the preferred spectral model. The pion-bump, a characteristic feature of the pion decay production mechanism of gamma rays, could be observed with the spectral parameters being similar to that of literature models as well as other analyses of IC 443. Thus a proton population and therefore interactions of the SNR with the surrounding molecular clouds is a scenario supported by the analysis, however leptonic gamma-ray production can not entirely be disregarded as it can contribute minorly to the observed spectrum.

In this work, only 11.4 h of observation time has been used and thus the analysis covered by the H.E.S.S. data is not very representative. This effects especially the spectral parameters and thus the physical model of the source and needs to be improved by future gamma-ray observations. The gap between the Fermi-LAT and IACT observations as well as high energy bands beyond the analysed IACT data can be covered by future observations conducted by the H.E.S.S. IACT array. This would improve the assessment of the physical model of the source significantly and therefore lead to a better understanding of IC 443.

Bibliography

[1] H. E. S. S. Collaboration, H. Abdalla, F. Aharonian, F. Ait Benkhali, et al. *Resolving the Crab pulsar wind nebula at teraelectronvolt energies*. Sept. 2019. DOI: 10.48550/arXiv.1909.09494.

[2] Jae-Joon Lee, Bon-Chul Koo, Min S. Yun, Snežana Stanimirović, et al. „A 21 cm SPECTRAL AND CONTINUUM STUDY OF IC 443 USING THE VERY LARGE ARRAY AND THE ARECIBO TELESCOPE“. English. In: *The Astronomical Journal* 135.3 (Mar. 2008), pp. 796–808. ISSN: 0004-6256, 1538-3881. DOI: 10.1088/0004-6256/135/3/796.

[3] The Fermi-LAT collaboration, M. Ackermann, M. Ajello, A. Allafort, et al. „Detection of the Characteristic Pion-Decay Signature in Supernova Remnants“. English. In: *Science* 339.6121 (Feb. 2013), pp. 807–811. ISSN: 0036-8075, 1095-9203. DOI: 10.1126/science.1231160.

[4] MAGIC Collaboration. „Discovery of VHE Gamma Radiation from IC443 with the MAGIC Telescope“. English. In: *The Astrophysical Journal* 664.2 (Aug. 2007), pp. L87–L90. ISSN: 0004-637X, 1538-4357. DOI: 10.1086/520957.

[5] V. A. Acciari, E. Aliu, T. Arlen, T. Aune, et al. „OBSERVATION OF EXTENDED VERY HIGH ENERGY EMISSION FROM THE SUPERNOVA REMNANT IC 443 WITH VERITAS“. English. In: *The Astrophysical Journal* 698.2 (June 2009), pp. L133–L137. ISSN: 0004-637X, 1538-4357. DOI: 10.1088/0004-637X/698/2/L133.

[6] J. J. L. Duyvendak. „FURTHER DATA BEARING ON THE IDENTIFICATION OF THE CRAB NEBULA WITH THE SUPERNOVA OF 1054 A.D. PART I. THE ANCIENT ORIENTAL CHRONICLES“. English. In: *Publications of the Astronomical Society of the Pacific* 54.318 (Apr. 1942), pp. 91–94. ISSN: 1538-3873. DOI: 10.1086/125409.

[7] William Parsons 3rd Earl of Rosse. „The Scientific transactions of the Royal Dublin Society“. English. In: *Royal Dublin Society* ser.2:v.2 (1879-1882).Volume 2 (1880), p. 47. URL: https://www.biodiversitylibrary.org/item/317633.

[8] Charles Messier. „Catalogue des Nébuleuses et des Amas d'Étoiles Observées à l'Observatoire de la Marine, hôtel de Clugni, rue des Mathurins“. French. In: *La Connaissance des temps, ou connaissance des mouvements célestes*. Paris: L'Imprimiere Royale, 1784, pp. 227–269.

[9] Maria Kuhn, Fanouria Antoniou, Enrico Bravin, Bernd Dehning, et al. „First LHC Emittance Measurements at 6.5 TeV“. In: Melbourne, Australia, 2016, pp. 562–566. ISBN: 978-3-95450-176-2. DOI: 10.18429/JACoW-IBIC2015-WEALA02.

[10] Duligur Ibeling and Alexander Heger. „THE METALLICITY DEPENDENCE OF THE MINIMUM MASS FOR CORE-COLLAPSE SUPERNOVAE“. English. In: *The Astrophysical Journal Letters* 765.2 (Feb. 2013). ISSN: 2041-8205. DOI: 10.1088/2041-8205/765/2/L43.

[11] Malcolm S. Longair. *High energy astrophysics*. English. 3rd ed. Cambridge ; New York: Cambridge University Press, 2011. ISBN: 978-0-521-75618-1. DOI: 10.1017/CBO9780511778346.

[12] Stefan Funk. „Ground- and Space-Based Gamma-Ray Astronomy“. English. In: *Annual Review of Nuclear and Particle Science* 65.1 (Oct. 2015), pp. 245–277. ISSN: 0163-8998, 1545-4134. DOI: 10.1146/annurev-nucl-102014-022036.

[13] Jeonghee Rho and R. Petre. „Mixed-Morphology Supernova Remnants“. English. In: *The Astrophysical Journal* 503.2 (July 1998). Publisher: IOP Publishing, p. L167. ISSN: 0004-637X. DOI: 10.1086/311538.

[14] R. A. Fesen. „The nature of the filaments northeast of the supernova remnant IC 443.“ In: *The Astrophysical Journal* 281 (June 1984), pp. 658–664. DOI: 10.1086/162142.

[15] Diego F. Torres, Gustavo E. Romero, Thomas M. Dame, Jorge A. Combi, and Yousaf M. Butt. „Supernova remnants and -ray sources“. In: *Physics Reports* 382.6 (Aug. 2003), pp. 303–380. ISSN: 0370-1573. DOI: 10.1016/S0370-1573(03)00201-1.

[16] Charles M. Olbert, Christopher R. Clearfield, Nikolas E. Williams, Jonathan W. Keohane, and Dale A. Frail. „A Bow Shock Nebula around a Compact X-Ray Source in the Supernova Remnant IC 443“. English. In: *The Astrophysical Journal* 554.2 (June 2001), pp. L205–L208. ISSN: 0004637X. DOI: 10.1086/321708.

[17] G. Castelletti, G. Dubner, T. Clarke, and N. E. Kassim. „High-resolution radio study of SNR IC443 at low radio frequencies“. In: *Astronomy & Astrophysics* 534:A21 (Oct. 2011). ISSN: 0004-6361, 1432-0746. DOI: 10.1051/0004-6361/201016081.

[18] E. Troja, F. Bocchino, and F. Reale. „XMM-Newton observations of the supernova remnant IC443: I. soft X-ray emission from shocked interstellar medium“. In: *The Astrophysical Journal* 649.1 (Sept. 2006), pp. 258–267. ISSN: 0004-637X, 1538-4357. DOI: 10.1086/506378.

[19] Joseph A. Esposito, Stanley D. Hunter, Gottfried Kanbach, and P. Sreekumar. „EGRET Observations of Radio-bright Supernova Remnants“. In: *The Astrophysical Journal* 461 (Apr. 1996), p. 820. ISSN: 0004-637X. DOI: 10.1086/177104.

[20] A. A. Abdo, M. Ackermann, M. Ajello, L. Baldini, et al. „OBSERVATION OF SUPERNOVA REMNANT IC 443 WITH THE FERMI LARGE AREA TELESCOPE“. English. In: *The Astrophysical Journal* 712.1 (Mar. 2010), pp. 459–468. ISSN: 0004-637X, 1538-4357. DOI: 10.1088/0004-637X/712/1/459.

[21] David J. Thompson and Colleen A. Wilson-Hodge. „Fermi Gamma-Ray Space Telescope“. English. In: *Handbook of X-ray and Gamma-ray Astrophysics*. Ed. by Cosimo Bambi and Andrea Santangelo. Singapore: Springer Nature, 2024, pp. 2383–2413. ISBN: 978-981-19696-0-7. DOI: 10.1007/978-981-19-6960-7_58.

[22] Heinrich J. Völk and Konrad Bernlöhr. „Imaging very high energy gamma-ray telescopes“. English. In: *Experimental Astronomy* 25.1 (Aug. 2009), pp. 173–191. ISSN: 1572-9508. DOI: 10.1007/s10686-009-9151-z.

[23] The HESS Collaboration and F. Aharonian. „Observations of the Crab Nebula with H.E.S.S“. English. In: *Astronomy & Astrophysics* 457.3 (Oct. 2006), pp. 899–915. DOI: 10.1051/0004-6361:20065351.

[24] Axel Donath, Régis Terrier, Quentin Remy, Atreyee Sinha, et al. „Gammapy: A Python package for gamma-ray astronomy“. English. In: *Astronomy & Astrophysics* 678 (Oct. 2023). Publisher: EDP Sciences, A157. ISSN: 0004-6361, 1432-0746. DOI: 10.1051/0004-6361/202346488.

[25] L. Mohrmann, A. Specovius, D. Tiziani, S. Funk, et al. „Validation of open-source science tools and background model construction in -ray astronomy“. English. In: *Astronomy &*

Astrophysics 632 (Dec. 2019). Publisher: EDP Sciences, A72. ISSN: 0004-6361, 1432-0746. DOI: 10.1051/0004-6361/201936452.

[26] Ti-pei Li and Yu-qian Ma. „ANALYSIS METHODS FOR RESULTS IN GAMMA-RAY ASTRONOMY“. English. In: *The Astrophysical Journal* 272.1 (1983).

[27] Hans Dembinski and Piti Ongmongkolkul et al. „scikit-hep/iminuit“. In: (2020). DOI: 10.5281/zenodo.3949207.

[28] Víctor Zabalza. *naima: a Python package for inference of relativistic particle energy distributions from observed nonthermal spectra*. English. Sept. 2015. URL: http://arxiv.org/abs/1509.03319.

[29] Daniel Foreman-Mackey, David W. Hogg, Dustin Lang, and Jonathan Goodman. „emcee: The MCMC Hammer“. In: *Publications of the Astronomical Society of the Pacific* 125.925 (Mar. 2013), pp. 306–312. DOI: 10.1086/670067.

[30] Ervin Kafexhiu, Felix Aharonian, Andrew M. Taylor, and Gabriela S. Vila. „Parametrization of gamma-ray production cross-sections for pp interactions in a broad proton energy range from the kinematic threshold to PeV energies“. English. In: *Physical Review D* 90.12 (Dec. 2014). arXiv:1406.7369. DOI: 10.1103/PhysRevD.90.123014.

Eigenständigkeitserklärung

Hiermit versichere ich, Lukas Großpietsch (22801606), die vorgelegte Arbeit selbstständig und ohne unzulässige Hilfe Dritter sowie ohne die Hinzuziehung nicht offengelegter und insbesondere nicht zugelassener Hilfsmittel angefertigt zu haben. Die Arbeit hat in gleicher oder ähnlicher Form noch keiner anderen Prüfungsbehörde vorgelegen und wurde auch von keiner anderen Prüfungsbehörde bereits als Teil einer Prüfung angenommen.

Die Stellen der Arbeit, die anderen Quellen im Wortlaut oder dem Sinn nach entnommen wurden, sind durch Angaben der Herkunft kenntlich gemacht. Dies gilt auch für Zeichnungen, Skizzen, bildliche Darstellungen sowie für Quellen aus dem Internet.

Mir ist insbesondere bewusst, dass die Nutzung künstlicher Intelligenz verboten ist, sofern diese nicht ausdrücklich als Hilfsmittel von dem Prüfungsleiter bzw. der Prüfungsleiterin zugelassen wurde. Dies gilt insbesondere für Chatbots (insbesondere ChatGPT) bzw. allgemein solche Programme, die anstelle meiner Person die Aufgabenstellung der Prüfung bzw. Teile derselben bearbeiten könnten.

Ort, Datum	Unterschrift